Thermophysical properties of hot fluid iron in the protolunar disk

Zhi Li, Razvan Caracas

Physics of the Earth and Planetary Interiors 321 (2021) 106806

Contents lists available at ScienceDirect

Physics of the Earth and Planetary Interiors

journal homepage: www.elsevier.com/locate/pepi

Thermophysical properties of hot fluid iron in the protolunar disk

Zhi Li [a,*], Razvan Caracas [a,b]

[a] CNRS, École Normale Supérieure de Lyon, Laboratoire de Géologie de Lyon UMR 5276, Centre Blaise Pascal, 46 allée d'Italie, 69364 Lyon, France
[b] The Center for Earth Evolution and Dynamics (CEED), University of Oslo, Blindern, Oslo, Norway

ARTICLE INFO

Keywords:
Proto-lunar disk
Thermophysical properties
Iron

ABSTRACT

We characterize the structural and transport properties of fluid iron at the low densities and high temperature conditions characteristic to the outer parts of protolunar disks, which form after giant impacts. We observe that decreasing the density and increasing the temperature decluster the fluid, which is eventually dominated by isolated atoms and dimers. In parallel, the electrical and thermal conductivities also decrease at a fast pace. The rapid diffusion enhances chemical equilibrium on large scales and the low viscosity favors turbulence in the disk.

1. Introduction

Iron is the major component of the core of telluric planets. As such, it naturally received significant attention from the geoscientific community, with the major effort put in understanding its behavior and properties in the high density and high temperature regions which are typical conditions for the Earth's core (126–360 GPa and 3500–6500 K). The structural (*e.g.* Campbell, 2016; Caracas, 2016), seismic (*e.g.* Steinle-Neumann et al., 2001; Vočadlo, 2007), thermodynamic (*e.g.* Alfè et al., 2000; Li et al., 2020; Vočadlo et al., 2003), thermochemical (Badro et al., 2016; Hirose et al., 2017) and transport (Gomi et al., 2013; de Koker et al., 2012; Pozzo et al., 2012) properties of iron and iron-based alloys were both measured experimentally and computed theoretically. Much less is known about the thermodynamic and thermophysical properties of iron below 1 GPa and above its melting point (around 1850 K). These conditions typically occur in the protoplanetary or protolunar disks (Canup, 2004) and during the release from large impacts (Kraus et al., 2015). Hixson et al. (1990) measured the liquid density and its electric conductivity at 0.2 GPa up to 4000 K by the pulse-heating technique. Assael et al. (2006) have compiled the available experimental data for the density and viscosity of iron up to 2500 K. But these efforts are still not enough to cover the entire range of thermodynamic conditions that may occur in a protolunar disk, and sometimes the incomplete information on the low density region may cause problems in our understanding of fundamental phenomena, like the formation of the Moon from the protolunar disk or the synestia. Kraus et al. (2015) used the dynamic shock compression technique to gain access to the high temperature and low-density regime, and they were able to locate the shock pressure needed to vaporize iron during giant impacts. Their experiments suggested a considerable amount of iron vapor was produced in the giant impacts, more than was previously estimated from an ANEOS equation of state (Pierazzo et al., 1997) that was less accurate in the low density regime. An even larger amount is suggested from the estimation of the entropy along the Hugoniot equation of state, as computed by *ab initio* simulations (Li et al., 2020), calculations that also determined the position of the critical point. The *ab initio* simulations suggested that the cores of small impactors from the late veneer completely vaporizes, and the core of Theia may have also partly vaporized. The rainout of the vaporized iron enhances the mixing and incorporation of metals in the mantle and thus may potentially affect the lithophile element budget in the mantle. In addition, a significant part of the iron vapor as well as the low-density high-temperature fluid would persist in the protolunar disk where it might contribute to its transport and chemical properties.

As it is extremely difficult to perform experiments in the low density and high temperature regime, *ab initio* molecular dynamics provide a reliable and relatively easy alternative to study this range of conditions. The simulations provide information on the thermodynamic, structural and transport properties at relevant density, temperature and pressure conditions. As the required computational resources increase considerably with the decreasing density, the simulations quickly become untractable. Consequently, here we focus on densities that are above 0.2 g/cm^3 and we characterize the structural and transport properties of iron including diffusion coefficients, viscosity and thermal conductivity.

* Corresponding author.
E-mail address: zhi.li@ens-lyon.fr (Z. Li).

https://doi.org/10.1016/j.pepi.2021.106806
Received 8 November 2020; Received in revised form 10 September 2021; Accepted 22 September 2021
Available online 28 September 2021

2. Computational details

2.1. Ab initio molecular dynamics

We performed *ab initio* molecular dynamics simulations using the VASP implementation (Kresse and Furthmüller, 1996a, 1996b). We employed the *NVT* ensemble, where the number of atoms, *N*, and the volume *V* of the unit cell, *i.e.* the density, are kept fixed, and the temperature *T* is controlled by a Nosé thermostat (Nosé, 1984). Our simulations contain 108 iron atoms. A Verlet algorithm is used to integrate the Newton's equation of motion with a timestep of 1 fs. The total simulation time at each temperature and density condition is at least 10 ps. The interatomic forces were calculated by the Hellmann-Feynman theorem within the framework of density functional theory (Hohenberg and Kohn, 1964; Kohn and Sham, 1965; Mermin, 1965) by employing the projector augmented wave (PAW) method (Blöchl, 1994; Kresse and Joubert, 1999). We employed the PBE formalism (Perdew et al., 1996) for the exchange correlation term; the valence electron configurations for the iron pseudopotential was $[Ar]3d^74s^1$. The partial occupancies of the electronic bands close to the Fermi level were calculated using a Fermi smearing scheme with a width at simulated temperature. The number of electronic bands was adapted to the temperature conditions such as to cover the entire spectrum of the fully and partially occupied states and to include enough non-occupied bands.

Before the production run, a convergence test has been done at 7.55 g/cm^3, the highest density covered in this study. For this, we first run a short MD simulation at this density and then select 38 snapshots separated by 100 fs. We found that, on average, the pressure computed with 550 eV for the cut-off energy and Gamma point to sample the Brillouin zone differs about 1 kbar from the one calculated with 850 eV and 4 × 4 × 4 k-points mesh generated by the Monkhorst-Pack scheme (Monkhorst and Pack, 1976). However, the total pressure including the kinetic energy contribution is around 12 kbar. Therefore, the error induced by the cut-off energy and k-points is less than its statistical fluctuation (20%). For energy, the difference is around 1.9 meV/atom. With decreasing density, the simulation cell becomes larger, causing a smaller basis vector in the reciprocal space. Therefore, with the fixed cut-off energy, more plane waves are included in the electronic structure calculation which provides a better accuracy. Thus, for the production run, we chose 550 eV as the cut-off energy and use the Gamma point to sample the Brillouin zone.

DFT simulations of iron and iron compounds at high density are typically in good agreement with experiments for a variety of properties, both liquid (Alfè et al., 1999; Gomi et al., 2013; Pozzo et al., 2012) and solid (Caracas, 2016). In the low-density and high-temperature regime there is a lack of both simulations and experiments to provide a reliable picture. We did tests on the Fe_2 dimer. We obtain a bond length in the range 2.000–2.004 Å regardless of the use or not of the van der Waals correlation, while experimental values are 2.02 +/− 0.02 Å (Leopold and Lineberger, 1986). Our harmonic vibrational frequencies are overestimated by about 20%.

2.2. Structural analysis

The short-range order in the fluid is revealed by the pair distribution function (PDF), $g_{Fe-Fe}(r)$:

$$g_{Fe-Fe}(r) = \frac{V}{N(N-1)} \left\langle \sum_i \sum_{j \neq i} \delta(r - r_{ij}) \right\rangle$$

where *r* is the correlation length and r_{ij} are the distance between atoms *i* and *j*, *N* is the total number of iron atoms in the simulations, and *V* is the volume of the simulation box.

2.3. The mean-squared displacement

The atomic mean-squared displacement (MSD) is defined as the average ⟨⟩ of the square of the distance travelled by the atoms *i* in a period of time τ, as:

$$MSD(\tau) = \langle [r_i(t_0 + \tau) - r_i(t_0)]^2 \rangle$$

The time origin t_0 is arbitrary. τ represents the width of a gliding time window that spans the trajectory. The values are averaged over the total number of atoms and time origins. From the slope of MSD, we can extract the diffusion coefficient *D* by exploiting the Einstein-Stokes equation, which have been reported in our previous work.

2.4. Velocity autocorrelation function

The normalized velocity autocorrelation function (VAF) is:

$$VAF(\tau) = \frac{\langle \boldsymbol{v}(0)\boldsymbol{v}(\tau) \rangle}{\langle \boldsymbol{v}(0)\boldsymbol{v}(0) \rangle}$$

where $\boldsymbol{v}(t)$ is the velocity of a particle at time τ and ⟨⟩ is computed as the time average over different time origins. The self-diffusion coefficient *D* is given by the time integral of the velocity autocorrelation function,

$$D = lim_{t \to \infty} \frac{1}{3} \int_0^t d\tau \langle \boldsymbol{v}(0)\boldsymbol{v}(\tau) \rangle$$

The self-diffusion coefficients obtained with the two methods should yield similar values.

2.5. Viscosity

The viscosity is given by the Green-Kubo formula,

$$\eta = \frac{V}{k_B T} \int_0^\infty \langle P_{\alpha\beta}(t) P_{\alpha\beta}(0) \rangle dt,$$

where *V* is the total volume, k_B is the Boltzmann constant, *T* is the temperature, $P_{\alpha\beta}$ stands for the off-diagonal element of the stress tensor and *t* denotes the correlation time.

2.6. Electrical and thermal conductivity

Here we only consider the electronic contribution to the electrical and thermal conductivities, as for metals it is the dominant part (Gomi et al., 2013; Pozzo et al., 2012). We calculate them using the Kubo-Greenwood formalism (Greenwood, 1958; Kubo, 1957) for 20 different configurations, equally spaced by 500 fs. This was successfully applied to liquid iron at the Earth's outer core conditions (Pozzo et al., 2012), and was shown to be considerably similar to results obtained from electron-phonon coupling (Gomi et al., 2013) at lower temperature. The Brillouin zone was sampled with the Baldereschi point (Baldereschi, 1973). A test with a grid of 4 × 4 × 4 k-points yields results within 1% difference in both types of conductivities to using only the Baldereschi point.

We calculate the dynamic Onsager coefficients, used in the estimation of the conductivity using the Kubo-Greenwood formula (Pozzo et al., 2012):

$$L_{lm}(\omega) = (-1)^{l+m} \frac{2\pi e^2 \hbar^2}{3m^2 \omega V} \sum_{\boldsymbol{k}} \sum_{i,j=1}^{n} \sum_{\alpha=1}^{3} w(\boldsymbol{k}) \left[f(\epsilon_{i,\boldsymbol{k}}) - f(\epsilon_{j,\boldsymbol{k}}) \right] \left| \langle \Psi_{j,\boldsymbol{k}} | \nabla_\alpha | \Psi_{i,\boldsymbol{k}} \rangle \right|^2 \left[\epsilon_{j,\boldsymbol{k}} - \mu \right]^{l-1} \left[\epsilon_{i,\boldsymbol{k}} - \mu \right]^{m-1} \delta(\epsilon_{j,\boldsymbol{k}} - \epsilon_{i,\boldsymbol{k}} - \hbar\omega)$$

where *e* and *m* are the electron charge and mass respectively, ω is the frequency, $\hbar$ is the reduced Plank's constant, *V* is the cell volume and *n* is the number of bands used in the simulations, α sum runs over the three spatial directions, $\Psi_{i,\boldsymbol{k}}$ and $\epsilon_{i,\boldsymbol{k}}$ are the Kohn-Sham wavefunctions and associated eigenvalues at the corresponding **k**-point, $f(\epsilon_{i,\boldsymbol{k}})$is the Fermi

factor. The δ function is represented by a Gaussian with width equal to the average spacing between the eigenvalues. $w(\boldsymbol{k})$ is the weight of the particular **k**-point in the Brillouin zone.

Then, using the Onsager coefficient, the electrical ($\sigma(\omega)$) and the thermal ($\kappa(\omega)$) conductivities are obtained as:

$$\sigma(\omega) = L_{11}(\omega)$$

and

$$\kappa(\omega) = \frac{1}{e^2 T}\left(L_{22}(\omega) - \frac{L_{12}(\omega)L_{21}(\omega)}{L_{11}(\omega)}\right)$$

The σ_0 and $\kappa_0$are the respective values of $\sigma(\omega)$ and $\kappa(\omega)$in the limit $\omega \rightarrow 0$.

In order to verify our implementation, we conducted simulations at 328 GPa and 6350 K for liquid iron using exactly the same parameters as (Pozzo et al., 2013). At these conditions, the density of liquid iron is 12.95 g/cm^3. We obtain an agreement better than 1% for both types of conductivity, thermal and electrical, when compared to the values reported in Pozzo et al., (2013).

3. Results and discussion

3.1. Phase diagram

In a previous study (Li et al., 2020), we bracketed the critical point of iron in the temperature range of 9000–9350 K and the density range of 1.85–2.40 g/cm^3, which corresponds to the pressure range of 4–7 kbars. We also calculated two Hugoniot lines that are up to 640 GPa and 22,000 K, and 830 GPa and 22,000 K, respectively. The computed entropy along these Hugoniot lines shows a steady increase up to 22.56 k_B/atom and 21.87 k_B/atom when reaching 640 GPa and 22,000 K, and 830 GPa and 22,000 K, respectively. In the following we analyze and discuss in detail the physical properties of iron, in the low-density high-temperature liquid and in the supercritical state.

3.2. Static structure

Fig. 1 shows snapshots of the fluid iron at several representative densities and temperatures. We observe a trend towards declustering

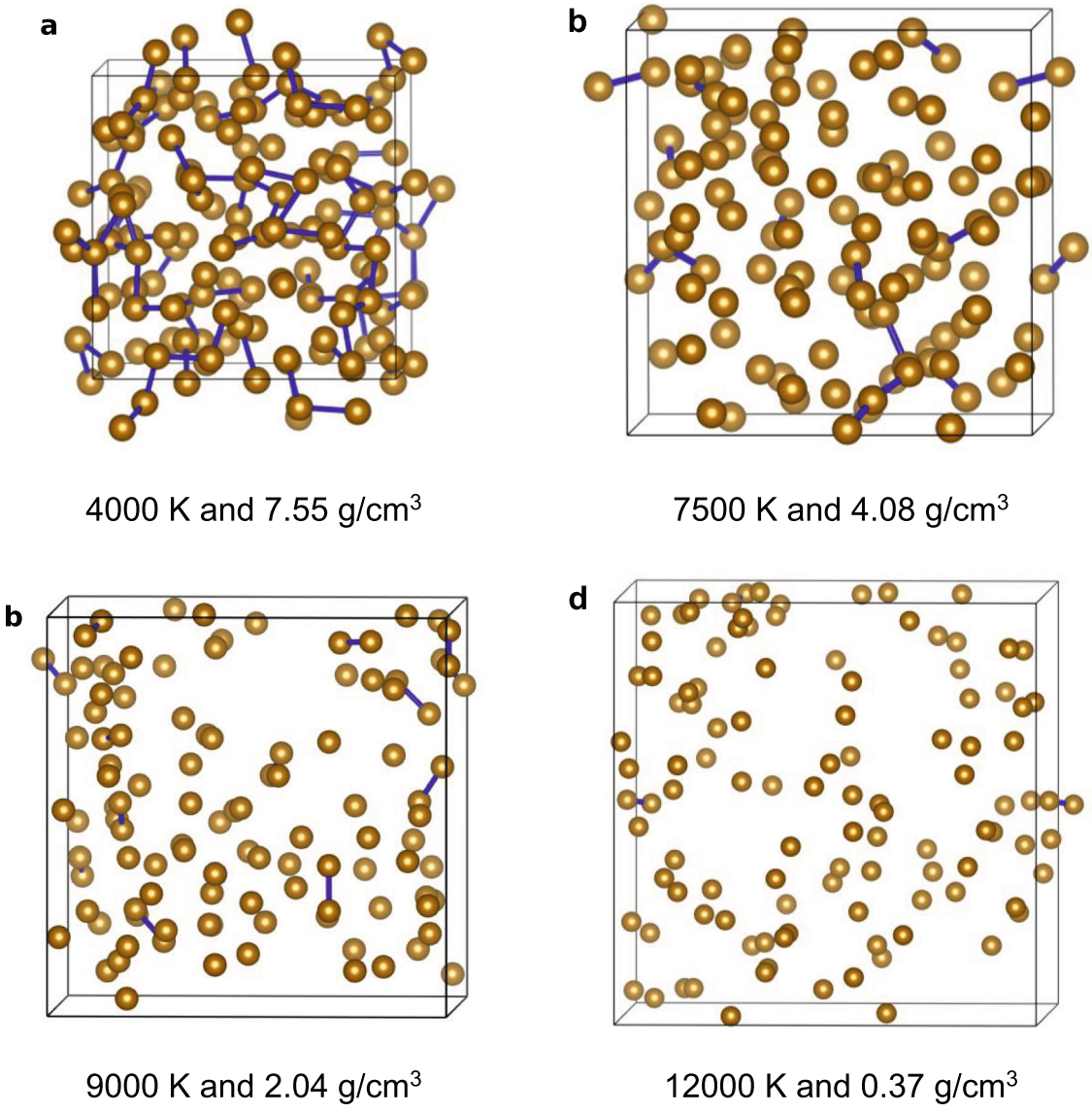

Fig. 1. Snapshots of the fluid iron at several temperature and density conditions. We observed a gradual de-polymerization with decreasing density and increasing temperature. At 12000 K and 0.37 g/cm^3, the dominant species is the isolated iron with only a minor amount of iron dimer.

with increasing temperature and decreasing density. This visual trend can be quantified by proper statistical analysis, as described in the following.

Several typical pair distribution functions (PDF) calculated from the MD simulations are shown in Fig. 2(a). As the periodic boundary condition is used, the maximum correlation length is limited to half of the cell length. All the interatomic PDFs start at zero, and continue as such up to a certain distance that defines the exclusion radius. This is caused by the strong repulsive force between any two atoms that prevents atoms from staying too close to each other. In the iron simulations, the exclusion radius depends weakly on the density and temperature; it decreases from 1.9 Å at 3000 K and 7.75 g/cm^3 to 1.8 Å at 12000 K and 0.37 g/cm^3 indicating a decline of repulsive force over this temperature and density regime.

The first peak in PDF, usually considered as a good approximation for the average bond distance in the fluid, occurs at 2.5 Å, with a height of 2.0 at 3000 K and 7.75 g/cm^3. These values remain relatively constant over a large range of temperature and density conditions, but the peak broadens with an increasing of temperature due to thermal activation. Previous *ab initio* molecular dynamics simulations at 1850 K and around 6.95 g/cm^3 also reported the main peak position of the PDFs at around 2.5 Å (Marqués et al., 2015).

The first minimum of the PDF marks the end of the first coordination sphere. At 3000 K and 7.75 g/cm^3, this lies at 3.3 Å and remains relatively constant over a large range of temperature and density conditions. We observe a second peak (the second coordination shell) at 4.5 Å, which again broadens with an increasing of temperature. Above 7500 K and below 2.70 g/cm^3, the positions of the first minimum and of the second peak become less obvious. And at 12000 K and 0.37 g/cm^3, the PDF decays steadily to a value close to one without an apparent minimum point. Due to the small cell size used here, we could not observe the long-distance behavior in PDF beyond 6 Å.

The integral of the PDF up to the first minimum gives the coordination numbers (CNs). The Fe-Fe coordination as a function of density and temperature is shown in Fig. 2(b). We observe a weak dependence of the coordination number with temperature. For example, at a density of about 6 g/cm^3, the coordination number decreases from about 11 at 3000 K down to about 9.5 at 7500 K, and by extrapolation down to about 8 at 12000 K. However, density has a more pronounced effect on the changes in coordination number. Along the 3000 K isotherm the coordination number increases from about 9.5 at about 6 g/cm^3 up to 13.5 at 8 g/cm^3. At 3000 K and 7.75 g/cm^3 (about 5 GPa in pressure) the coordination is around 13.6, indicating a very close-packed liquid. Actually the value of 14 seems to be a saturation value for coordination in liquid iron at high pressures and densities, *i.e.* at 6000 K and 13.3 g/cm^3, the conditions at inner-outer core boundary inside the Earth, as was shown in other previous *ab initio* MD studies (Alfè et al., 2000; Vočadlo et al., 1997). The change in slope around 7.75 g/cm^3 implies that probably the compression mechanism above this density is likely to be caused by the change in the second coordination shell. With decreasing density along the same isotherm, the Fe-Fe coordination decreases to around 10.8 at a density of 5.81 g/cm^3. In the supercritical region, at 12000 K, the Fe-Fe coordination drops from 6.3 at 2.7 g/cm^3 density to 1.6 at 0.37 g/cm^3. A change in slope of the density-coordination dependence occurs around 1.46 g/cm^3 along 12,000 K. At the critical point, the Fe-Fe coordination number is around 6.

3.3. Speciation

The coordination number as obtained from PDF only gives an average information on the number of atoms that surrounds a central iron atom. The distribution of the bond lengths and the lifetimes of atomic clusters are still missing. Consequently, we also use a geometric criterion to analyze the interatomic connectivity at every configuration generated during our simulations. The geometric cut-off length for two atoms to be considered connected, *i.e.* bonded, is chosen to be the radius of the first coordination sphere that is the first minimum of PDF. Then the size of any given iron coordination polyhedron is defined as the number of atoms within the range of the first minimum of PDF. Once the individual atoms forming a given coordination polyhedron are identified, we monitor the time they obey the geometrical criterion for bonding to define the polyhedron lifetime.

Fig. 3(a) shows the coordination of atoms at different conditions. In general, we observe, as expected, a declustering of the fluid with decreasing temperature. At 3000 K, from 7.97 g/cm^3 to 6.78 g/cm^3, the iron is highly polymerized with few or no isolated Fe atoms. With further decrease of density, we observe the presence of isolated Fe atoms with an increasing abundance from 0.02 at 6.78 g/cm^3 to 0.15 at 5.81 g/cm^3

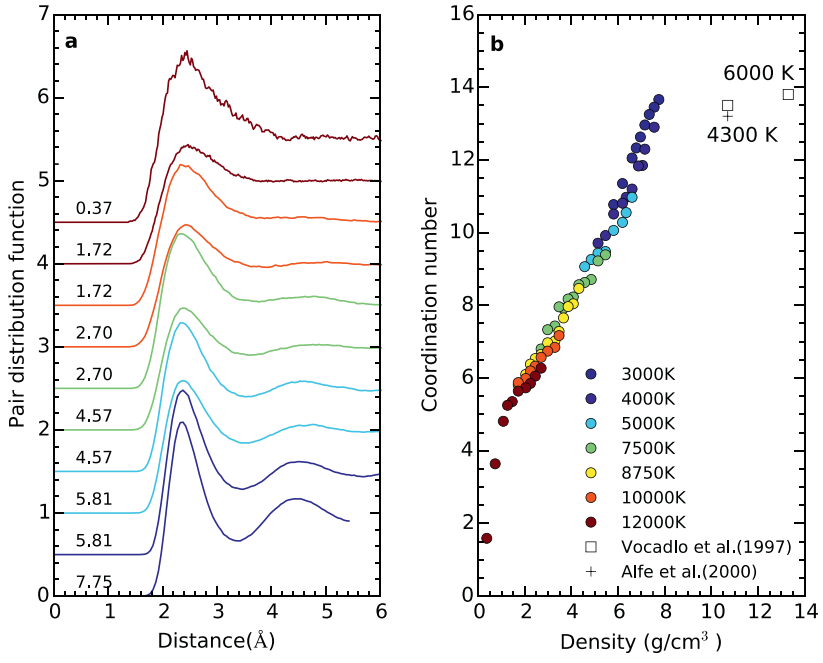

Fig. 2. The static structure of hot fluid iron. (**a**) Pair distribution function for iron at selected temperatures and densities. The color of solid lines represents different temperatures, as shown in the legend of (**b**). The unit is g/cm^3. (**b**) The coordination number calculated by counting the number of atoms within the first minimum of *g(r)* from a central atom. There is a weak dependence of the coordination number with the temperature. However, its density dependence is very strong below 7.75 g/cm^3, then saturates at a value of 13 up to 6000 K and 13.3 g/cm^3 (Alfè et al., 2000; Vočadlo et al., 1997), which is corresponds to the Earth's inner-outer core boundary.

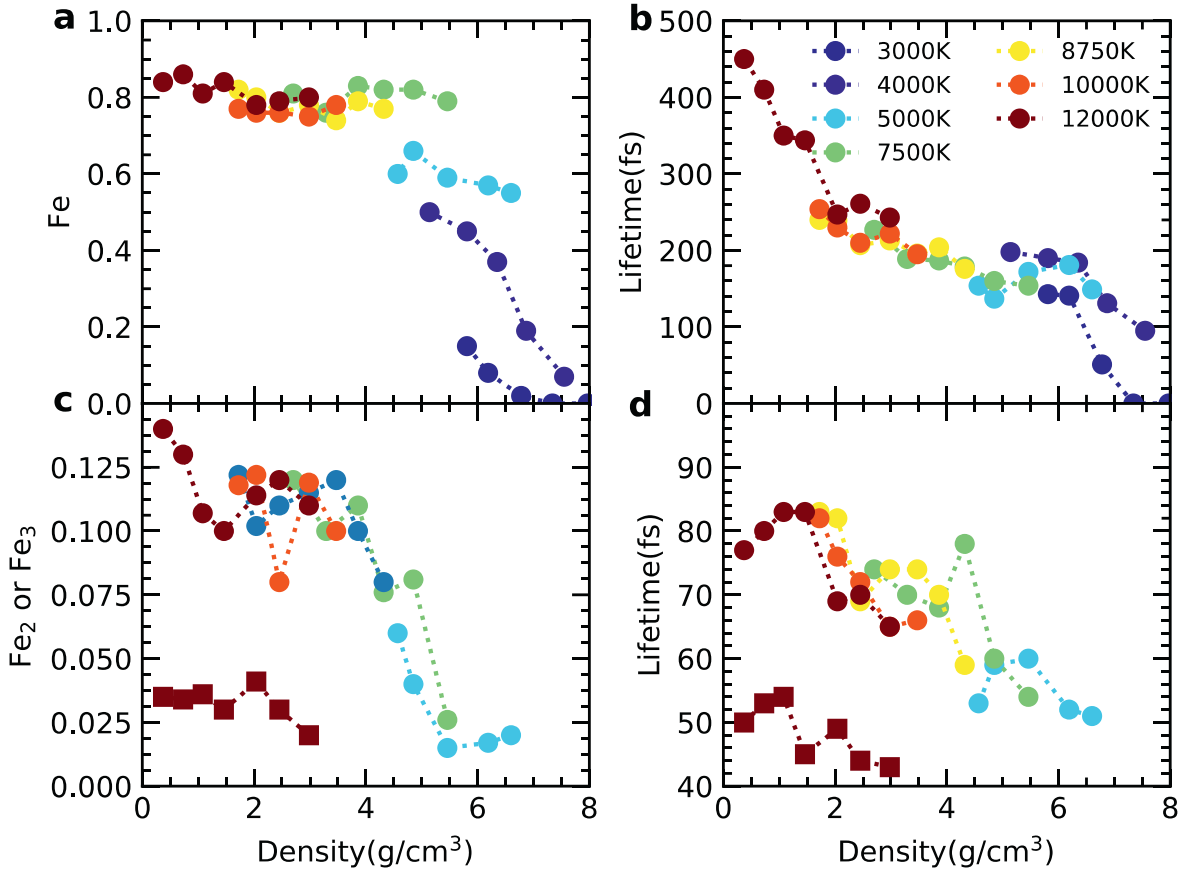

Fig. 3. Speciation of isolated clusters of hot fluid iron at low densities and high temperatures, representing a good approximant to the structure of the gaseous iron. In **(a)** and **(b)**, the relative abundance and the average lifetimes of isolated iron atoms are displayed. In **(c)** and **(d)**, we have shown the abundance and lifetimes of iron dimers (Fe_2) represented by the circles, and iron trimers (Fe_3) in squares. Other clusters are not shown as their abundance are below 0.005. In the supercritical regime (10,000 K and 12,000 K), the iron fluid is dominated by long-lived monoatomic and diatomic clusters; at low temperatures we retrieve more familiar polymerized melts.

indicating a gradual declustering. Along the 4000 K isotherm, the abundance of isolated iron atoms increases rapidly from 0.07 at 6.78 g/cm^3 to 0.50 at 5.14 g/cm^3. Above 7500 K and below 5.46 g/cm^3, we observe a nearly constant concentration of 0.85 of isolated iron atoms, irrespective of the temperature. The lifetime of isolated Fe atoms is shown in Fig. 3(b); in general, the increase of temperature and the increase of density result in decreasing their lifetime. In the supercritical regime, at 12000 K, the lifetime of isolated atoms increases linearly with decreasing the density. At the lowest density of 0.37 g/cm^3 calculated in the present study, the lifetime is around 450 femtoseconds. We also observed some small Fe_2 dimers starting to appear from 5000 K and 6.60 g/cm^3, as illustrated in Fig. 3(c). There is a weak temperature dependence of the Fe_2 abundance, with a major role played by the density. The abundance of Fe_2 clusters increases considerably in the 5.46 to 4.32 g/cm^3 density range. Below 5.46 g/cm^3 density, the abundance of Fe_2 fluctuates around 0.11 until 1.08 g/cm^3, then increases again to 0.14 at further decreasing density to 0.37 g/cm^3. We only find a small amount of iron trimers (Fe_3) at 12000 K. The lifetime of Fe_2 and Fe_3 clusters (Fig. 3(d)) is below 100 femtoseconds, shorter than that of Fe. Our results suggest the critical iron fluid is mainly atomic with the Fe dimers being the next most abundant species.

3.4. Velocity autocorrelation function

As a time-dependent correlation function, the velocity autocorrelation function (VAF) not only reveals the underlying dynamical processes like diffusional and vibrational motions operating in an atomic or molecular system at a microscopic scale, but also shows a direct connection with the macroscopic properties like the diffusion coefficient. These facts offer a good reason to study VAF, whose straightforward calculation details are provided in Section 2.4. We plot the overall trend from 3000 K and 7.75 g/cm^3 to 10,000 K and 3.86 g/cm^3 in Fig. 4(a). At 7.65 g/cm^3 and 3000 K, VAF decays to reach a first minimum at a value of 80 fs. The formation of this first minimum is generally attributed to the cage effect formed by the nearest neighbors, which exert a restoring opposite force on the central atom when this encounters its cage during the vibration. There are two more minima at larger correlation times. Globally, the three observed minima represent different vibrational modes. With further decreasing density to 5.81 g/cm^3 at 3000 K, as the atoms become increasingly spaced, only two minima are found, and their positions are shifted to longer correlation times (*i.e.* low frequency) due to a decrease of the interaction strength (also see Fig. 5). With increasing temperature at fixed density of 5.81 g/cm^3, the minimum becomes less obvious and disappears at 7500 K where a single exponential decay is present, indicating the cage structure can no longer hold the Fe atoms due to the large thermal velocity at high temperature. The VAF decay is weakly dependent on temperature, but appears at relatively similar densities.

To illustrate the dependence of the VAF with the density, we show its variation along the 12,000 K isotherm in Fig. 4(b). The decay of VAF becomes faster at high densities since collisions occur more frequently due to the relatively short distances between atoms, which break

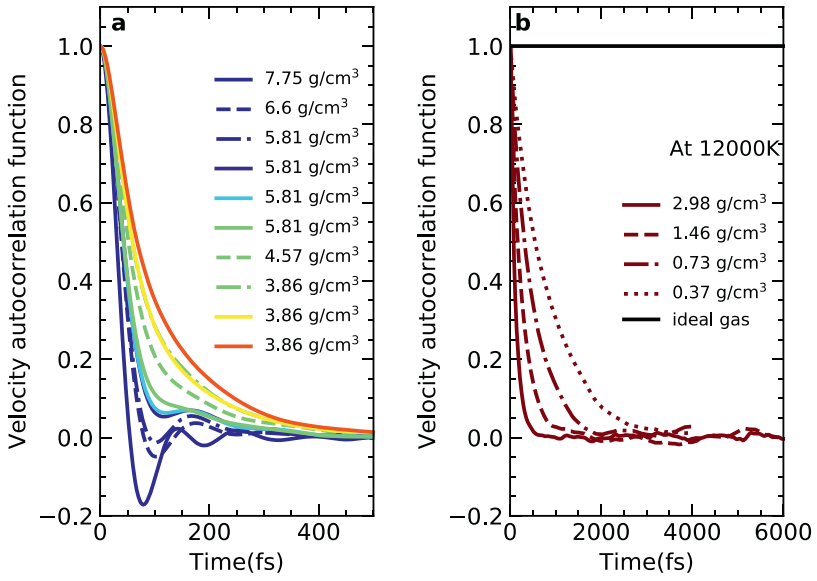

Fig. 4. (**a**) The overall trend of velocity autocorrelation function from 3000 K and 7.75 g/cm^3 to 10,000 K and 3.86 g/cm^3. (**b**) Velocity autocorrelation function along the supercritical isotherm 12,000 K as a function of density. With decreasing density, the behavior of fluid iron approaches that of a dense ideal gas because of the absence of interactions. Therefore, the velocity autocorrelation function always keeps at a constant value of 1.0, as the initial velocity are not altered with time.

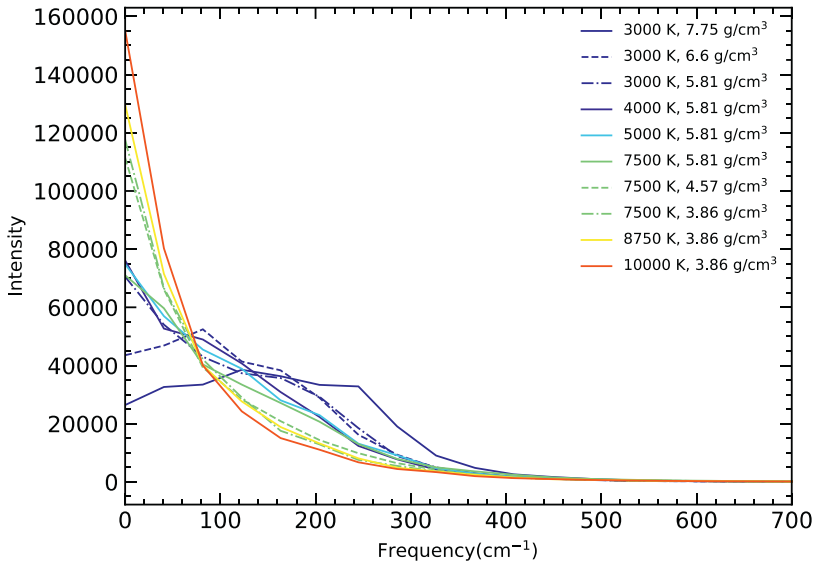

Fig. 5. Vibrational spectrum of fluid iron calculated by Fourier transform of the velocity autocorrelation function shown in Fig. 4 (a). At 3000 K and 7.75 g/cm^3, we observe a broad peak from 0 to 400 cm^{-1}, which is caused by breathing-types vibrations of the first coordination shell.

correlations. The decay time of VAF at 12000 K and 0.37 g/cm^3 is around 2500 fs, suggesting that at these conditions, only 12 independent configurations are sampled during a 30 ps simulation. The situation would become even worse when the temperature and density are below 12,000 K and 0.37 g/cm^3 since the correlation time increases with decreasing temperature and density. Reed and Flurchick (1994) found the statistical inefficiency, which represents the average time needed to sample two statistically uncorrelated configurations during an MD simulation, is almost linearly scaling with the inverse of density. For the low-density phase, an intrinsic problem is that there are two time scales: the inter-collision time and collision duration. As the collision duration is very short, the atoms move in space for a very long time before the next collision occurs. A common method to speed up the correlation time is to use a larger time step. But a very large time step would cause missing collisions and thus decreasing accuracy of sampling of the configurational space. Reed and Flurchick (1994) proposed a hybrid algorithm that combines the time-driven simulation with event-driven simulation, which is frequently used in the hard-sphere models. This may provide a promising solution to the time scale problems. However, many questions need to be answered before its practical implementations combined with density functional theory will become available, especially on how to define a collision radius.

3.5. Diffusion

The mean square displacements (MSD) measure the average distance that atoms move during a reference time window. We show in Fig. 6 four examples that cover the whole studied temperature range from 3000 to

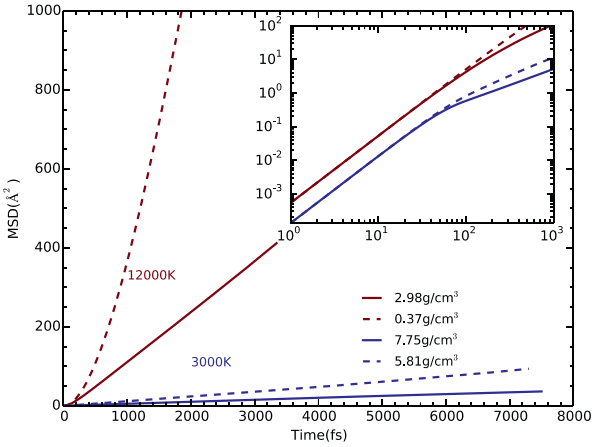

Fig. 6. The mean-squared displacement (MSD) of fluid iron at selected densities and temperatures. The inset shows a log-log zoom-in plot for short times. The inset outlines a slope change that separates the two characteristic regions of the diffusion: ballistic, for times less than about 100 fs, and diffusive, at higher times.

12,000 K and density range from 7.75 to 0.37 g/cm^3. The total diffusion process can be divided into two stages, as seen by the change of slope in the log-log plot in the inset in Fig. 6. The first part, on the order of about 100 fs, is the ballistic part dominated by the free particle motion before collision. The second part is dominated by the diffusion of the particles; in this region the square displacement linearly scales as the function of time. The slope of the MSD yields the diffusion coefficient *via* a prefactor of 1/(2n), where n is the number of degrees of freedom per atom, which is 3 in our case.

We also calculate the diffusion coefficient by integrating the velocity autocorrelation function, as shown in Fig. 7. The diffusivity increases by two orders of magnitude from about 1.0×10^{-8} m^{2}s^{-1} at 7.75 g/cm^3 and 3000 K to about 1.3×10^{-6} m^{2}s^{-1} at 0.37 g/cm^3 and 12,000 K. We estimate its uncertainty by dividing the total simulation into several

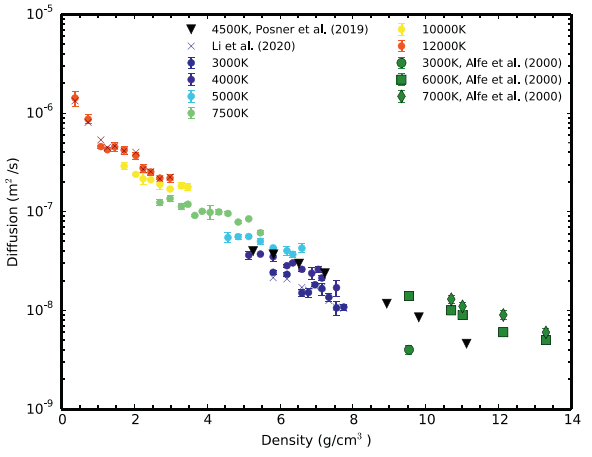

Fig. 7. The temperature and density dependence of the self-diffusion coefficients of fluid iron. The solid circles and black crosses represent diffusivities determined from velocity autocorrelation function and mean-squared displacement (Li et al., 2020), respectively. The green squares and black triangles denote several self-diffusion coefficients of liquid iron at high densities and temperatures previously reported in the literature. (For interpretation of the references to color in this figure legend, the reader is referred to the web version of this article.)

blocks of 2 ps for simulations at 3000 K and 7.75 g/cm^3 since the velocity autocorrelation function decays to zero at this time length. The resulting uncertainly is about 22% of the diffusivity value. At high densities and low temperatures, the diffusion coefficients correspond to distances travelled by the iron atoms on the order of about 2.5 cm in 24 h, which would ensure highly efficient chemical equilibration close to the surface of the iron droplets. At low densities and high temperatures, the diffusion coefficients correspond to displacements on the order of 0.5 m in 24 h, which would contribute significantly to the chemical equilibration inside large-scale fluid volumes. As expected, the increasing temperature and decreasing density would increase the diffusivity. There is an excellent agreement between the values of the diffusion coefficients obtained using the two methods (the slope of the MSD and the integration of the VAF). Our values also compare well with previous theoretical studies in liquid iron (Alfè et al., 2000; Posner et al., 2017), at higher pressures and lower temperatures.

3.6. Viscosity

The viscosity of iron was computed previously only in its high-density liquid state (Alfè et al., 2000; de Wijs et al., 1998) and applied to the dynamics of the liquid outer core of the Earth. We obtain the viscosity from the self-correlation of the shear components stress tensor. As a general rule this method requires much longer simulations times than are needed to obtain the other properties. We can improve a little the quality of the results by averaging over all the three shear components of the stress tensor. Fig. 8(a) displays the stress autocorrelation function (SAF) for fluid iron at 3000 K and 7.75 g/cm^3. After 0.15 ps, SAF decays to zero with a still large noise, about 5% compared with the value at $t = 0$. The inset in Fig. 8(a) shows the viscosity integral as a function of time. After 0.4 ps, the shear viscosity fluctuates within the range 3×10^{-3}–5×10^{-3} Pa s. We estimate the standard deviation to about 40% of the total value of viscosity by dividing and analyzing the total simulation in several blocks of 2 ps, a time length that corresponds to the decay of the correlations function.

We present the variation of viscosity as a function of density along several isotherms in Fig. 8(b). The values of viscosity at conditions typical to the outer parts of the protolunar disk, *i.e.* low density and high temperature, are in the range 0.5×10^{-3} to 4×10^{-3} Pa s. They show a decreasing trend with decreasing density, but due to the large scatter in values, we cannot identify any reliable trend with temperature. The values that we obtain for conditions specific to the protolunar disk are one order of magnitude smaller than in the Earth's outer core, estimated to be on the order of 2×10^{-3}–15×10^{-3} Pa s (Alfè et al., 2000; de Wijs et al., 1998). Assael et al., (2006) compiled viscosity data for liquid iron from 1850 K and 7.0 g/cm^3 to 2500 K and 6.40 g/cm^3. We find the viscosity at 3000 K and 6.40 g/cm^3 of 2.1×10^{-3} Pa s to be comparable to the corresponding value at 2500 K and 6.40 g/cm^3 of 2.276×10^{-3} Pa s (Assael et al., 2006).

At 3000 K and 7.75 g/cm^3 we perform a further check and compute the viscosity using the Stoke-Einstein relations, which connects diffusion coefficient to estimate the viscosity:

$$\eta = \frac{k_B T}{2\pi a D}$$

where η is the viscosity, k_B is the Boltzmann constant, T is temperature, D is the diffusion coefficient and a is the effective atomic diameter. Because iron is a metallic monoatomic fluid that does not form long-lasting structural units, we followed previous studies (de Wijs et al., 1998) and choose the value of the effective atomic radius to be the first peak in the radial distribution function. This method has been used previously to determine the viscosity of liquid iron at Earth's core conditions (de Wijs et al., 1998). By applying this method, the estimate viscosity is 3×10^{-3} Pa s, in remarkable agreement with the Green-Kubo method.

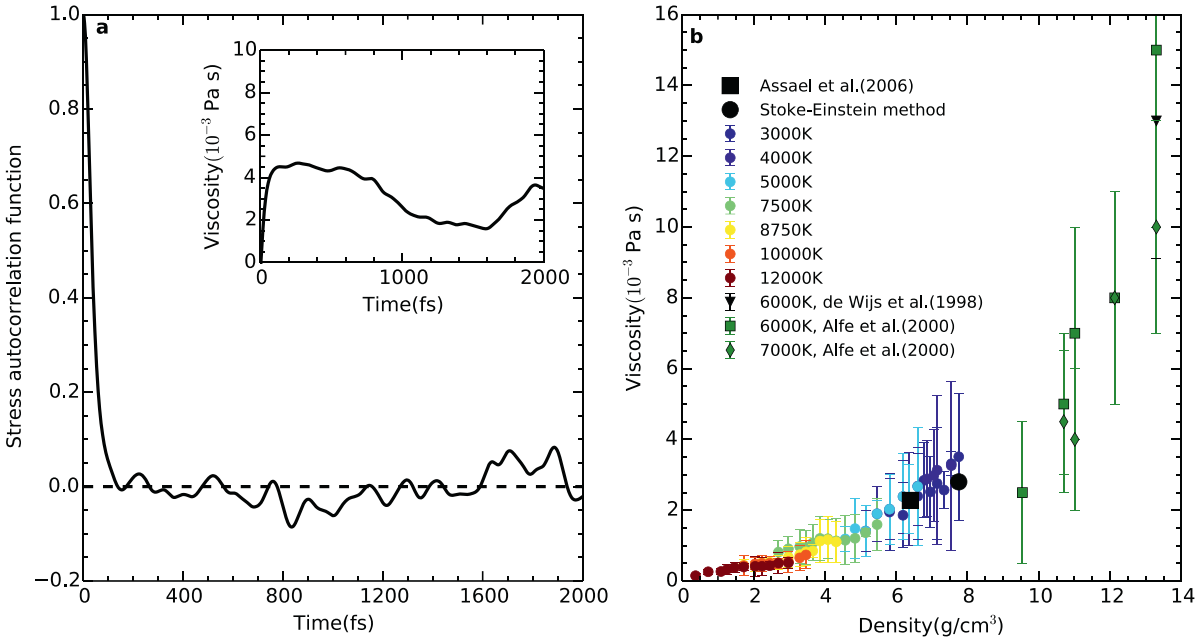

Fig. 8. Viscosity of fluid iron varying as a function of temperature and density. (**a**) Stress autocorrelation function for fluid iron at 3000 K and 7.75 g/cm^3 calculated by averaging over three off-diagonal stress tensor and normalizing by dividing the value at time zero. The inset shows viscosity integral of the average stress autocorrelation function as a function of time. The shaded areas denote the fluctuation of the viscosity. (**b**) The overall overview of viscosity of fluid iron as a function of temperature and density. The black square represents an experimental value at 2500 K and 6.40 g/cm^3 (Assael et al., 2006), which is close to our 3000 K isotherm. The black solid circles are the viscosity at 3000 K and 7.75 g/cm^3 determined from the Stoke-Einstein relation, which is in a fair agreement with the prediction by the Green-Kubo method. (For interpretation of the references to color in this figure legend, the reader is referred to the web version of this article.)

3.7. Electric and thermal conductivity

Next we used the Kubo-Greenwood formalism (Greenwood, 1958; Kubo, 1957) to determine the electrical and thermal conductivities. In this method, the electron-ion collisions are accurately described, while the electron-electron scattering and is neglected and its effect remains unclear (Dufty et al., 2018). Fig. 9 shows the computed electrical and thermal conductivities, and the Lorentz constant of pure fluid iron as a function of density and temperature. Both the electrical and the thermal conductivities decrease monotonically with decreasing density, as the fluid declusters and is gradually dominated by isolated dimers and single atoms, causing electrons to become more localized. Along the 3000 K isotherm, the electrical conductivity decreases from 1.2×10^6 Ω^{-1} m^{-1} at 7.76 g/cm^3 to 0.8×10^6 Ω^{-1} m^{-1} at 5.81 g/cm^3, while the thermal conductivity decreases from 80 Wm^{-1} K^{-1} to 40 Wm^{-1} K^{-1}.

At densities above 6.19 g/cm^3, iron behaves like a typical metal, with the electrical conductivity decreasing with increasing temperature, which enhances the electron-ion collisions. Below 6.19 g/cm^3, the trend is reversed, with the electrical conductivity increasing with temperature. It indicates the fluid iron at low-density conditions behaves more like a semiconductor, where the temperature dependence may as well be a result of the increasing concentration of carriers due to thermal excitation. The observed change of the temperature dependence around 6.19 g/cm^3 suggests a possible metal-non-metal transition and has also been observed in other expanded metals like aluminium (Recoules et al., 2002). The calculated Lorentz number, which represents the ratio between the thermal and the electrical conductivity (Fig. 9(c)) is almost constant and close to its ideal value of 2.44×10^{-8} WΩK^{-2} over the whole temperature and density ranges studies.

4. Conclusions

Hydrodynamic simulations, shock experiments, and *ab initio* simulations showed that during the giant impact most of the core of the impactor Theia lost its integrity and was dispersed in the protolunar disk. The droplets of fluid iron that reached the outer parts of the disk were at high temperature and low density, in a state of supercritical fluid or hot vapor. In the inner region of the disk, where the impact deposited a considerable amount of energy, the core of the proto-Earth was at high density and high temperature, probably in supercritical state. These different physical states see different thermodynamic and kinetic behaviors.

Here we investigate the structural and transport properties of iron from *ab initio* molecular dynamics simulations at densities below 7.8 g/cm^3 and up to 12,000 K, conditions typical for the outer parts of the protolunar disk. We find that the low-density fluid is highly declustered, its structure dominated by isolated atoms and dimers. The polymerization and the coordination number increase strongly with density below 7.75 g/cm^3, then saturates at a value of ~14 that persists at least up to 6000 K and 13.3 g/cm^3, which is the condition at the Earth's inner-outer core boundary.

At the high temperatures of the protolunar disk, the diffusion coefficients are on the order of 10^{-7} to 10^{-6} m^2/s. As the temperature drops, the diffusion slows down, losing almost one order of magnitude down to 3000 K. But throughout the potential lifetime of the iron droplets in the protolunar disk, the diffusion coefficients should be sufficiently fast to promote chemical equilibration over multiple centimeters distances in a matter of only hours.

The viscosity of iron in the outer parts of the protolunar disk is also extremely low, on the order of 10^{-3} Pa s, which is one order of magnitude smaller than the value in the Earth's liquid outer core (de Wijs et al., 1998). A low viscosity implies a limited role in the global energy budget of the disk, a term oftentimes neglected in magneto-hydrodynamic simulations (Breuer et al., 2015), and a possible presence of turbulence as the primary mechanism of transporting mass in the disk.

Finally, the computed electronic and thermal conductivities decrease with the density, suggesting a gradual reduction of the metallic character. We do not observe any discontinuity in the density dependence of

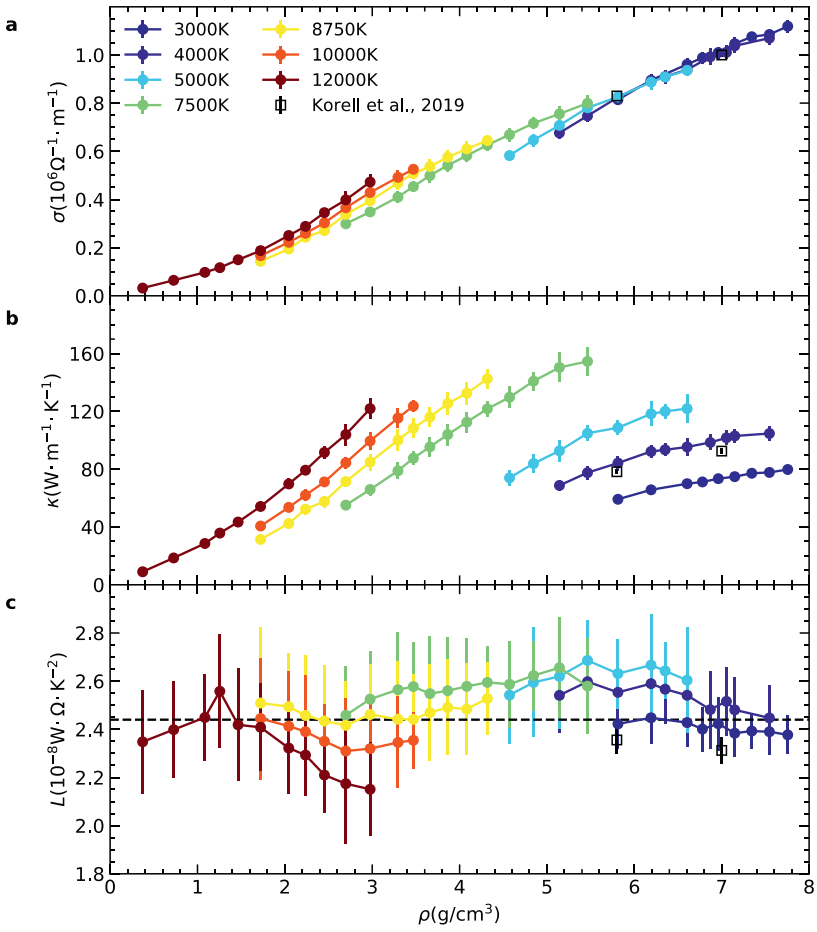

Fig. 9. Electrical conductivity (**a**), thermal conductivity (**b**) and Lorentz number (**c**) of the fluid iron as a function of density and temperature. The Lorentz number is defined as $L = \kappa/\sigma T$. The results from our work are represented as solid circles color-coded as a function of temperature. The theoretical results at around 3500 K and 6.22 g/cm^3 are from Korell et al., (2019), shown as black squares. The black dashed line in (**c**) represented the ideal Lorentz number of 2.44.

the electric conductivity. The only visible effect is that the electric conductivity falls more rapidly as the density decreases below 5.14 g/cm^3. Around the critical point the thermal conductivity is around 10 Wm^{-1} K^{-1}, similar to the value of silicates in the lower mantle conditions (Stackhouse et al., 2015).

Further simulations of the geodynamical evolution of the protolunar disk will need to incorporate these numerical values for iron at the relevant thermodynamic conditions of the disk. Such simulations can determine the cooling rates of the disk, the condensation trajectories for both the Earth and the Moon, and the multiscale chemical mixing between the mantle and the core.

Author statement

ZL and RC proposed the research. ZL performed the calculations. ZL and RC analyzed the data and wrote the paper.

Declaration of Competing Interest

The authors declare that they have no known competing financial interests or personal relationships that could have appeared to influence the work reported in this paper.

Acknowledgments

This research was supported by the European Research Council (ERC) under the European Union's Horizon 2020 research and innovation program (grant agreement no. 681818 IMPACT to RC). We acknowledge access to the GENCI supercomputers (Occigen at CINES, Ada and Jean-Zay at IDRIS, and Curie and Irene at TGCC) through the stl2816 series of eDARI computing grants, the PRACE grant RA4947 and the Uninet2 NN9697K grant.

References

Alfè, D., Gillan, M.J., Price, G.D., 1999. The melting curve of iron at the pressures of the Earth's core from ab initio calculations. Nature 401, 462–464. https://doi.org/10.1038/46758.

Alfè, D., Kresse, G., Gillan, M.J., 2000. Structure and dynamics of liquid iron under Earth's core conditions. Phys. Rev. B 61, 132–142. https://doi.org/10.1103/PhysRevB.61.132.

Assael, M.J., Kakosimos, K., Banish, R.M., Brillo, J., Egry, I., Brooks, R., Quested, P.N., Mills, K.C., Nagashima, A., Sato, Y., Wakeham, W.A., 2006. Reference data for the density and viscosity of liquid aluminum and liquid iron. J. Phys. Chem. Ref. Data 35, 285–300. https://doi.org/10.1063/1.2149380.

Badro, J., Siebert, J., Nimmo, F., 2016. An early geodynamo driven by exsolution of mantle components from Earth's core. Nature 536, 326–328. https://doi.org/10.1038/nature18594.

Baldereschi, A., 1973. Mean-value point in the Brillouin zone. Phys. Rev. B 7, 5212–5215. https://doi.org/10.1103/PhysRevB.7.5212.

Blöchl, P.E., 1994. Projector augmented-wave method. Phys. Rev. B 50, 17953–17979. https://doi.org/10.1103/PhysRevB.50.17953.

Breuer, D., Rueckriemen, T., Spohn, T., 2015. Iron snow, crystal floats, and inner-core growth: modes of core solidification and implications for dynamos in terrestrial planets and moons. Prog. Earth Planet. Sci 2 (39). https://doi.org/10.1186/s40645-015-0069-y.

Campbell, A.J., 2016. Phase diagrams and thermodynamics of Core materials. In: Terasaki, H., Fischer, R.A. (Eds.), Geophysical Monograph Series. John Wiley & Sons, Inc, Hoboken, NJ, pp. 191–199. https://doi.org/10.1002/9781118992487.ch15.

Canup, R.M., 2004. Simulations of a late lunar-forming impact. Icarus 168, 433–456. https://doi.org/10.1016/j.icarus.2003.09.028.
Caracas, R., 2016. Crystal structures of Core materials. In: Terasaki, H., Fischer, R.A. (Eds.), Geophysical Monograph Series. John Wiley & Sons, Inc, Hoboken, NJ, pp. 55–68. https://doi.org/10.1002/9781118992487.ch5.
de Koker, N., Steinle-Neumann, G., Vlček, V., 2012. Electrical resistivity and thermal conductivity of liquid Fe alloys at high P and T, and heat flux in Earth's core. Proc. Natl. Acad. Sci. 109, 4070–4073. https://doi.org/10.1073/pnas.1111841109.
de Wijs, G.A., Kresse, G., Vočadlo, L., Dobson, D., Alfè, D., Gillan, M.J., Price, G.D., 1998. The viscosity of liquid iron at the physical conditions of the Earth's core. Nature 392, 805–807. https://doi.org/10.1038/33905.
Dufty, J., Wrighton, J., Luo, K., Trickey, S.B., 2018. On the Kubo-Greenwood model for electron conductivity. Contrib. Plasma Phys. 58, 150–154. https://doi.org/10.1002/ctpp.201700102.
Gomi, H., Ohta, K., Hirose, K., Labrosse, S., Caracas, R., Verstraete, M.J., Hernlund, J.W., 2013. The high conductivity of iron and thermal evolution of the Earth's core. Phys. Earth Planet. Inter. 224, 88–103. https://doi.org/10.1016/j.pepi.2013.07.010.
Greenwood, D.A., 1958. The Boltzmann equation in the theory of electrical conduction in metals. Proc. Phys. Soc. 71, 585–596. https://doi.org/10.1088/0370-1328/71/4/306.
Hirose, K., Morard, G., Sinmyo, R., Umemoto, K., Hernlund, J., Helffrich, G., Labrosse, S., 2017. Crystallization of silicon dioxide and compositional evolution of the Earth's core. Nature 543, 99–102. https://doi.org/10.1038/nature21367.
Hixson, R.S., Winkler, M.A., Hodgdon, M.L., 1990. Sound speed and thermophysical properties of liquid iron and nickel. Phys. Rev. B 42, 6485–6491. https://doi.org/10.1103/PhysRevB.42.6485.
Hohenberg, P., Kohn, W., 1964. Inhomogeneous electron gas. Phys. Rev. 136, B864–B871. https://doi.org/10.1103/PhysRev.136.B864.
Kohn, W., Sham, L.J., 1965. Self-consistent equations including exchange and correlation effects. Phys. Rev. 140, A1133–A1138. https://doi.org/10.1103/PhysRev.140.A1133.
Korell, J.-A., French, M., Steinle-Neumann, G., Redmer, R., 2019. Paramagnetic-to-diamagnetic transition in dense liquid iron and its influence on electronic transport properties. Phys. Rev. Lett. 122, 086601 https://doi.org/10.1103/PhysRevLett.122.086601.
Kraus, R.G., Root, S., Lemke, R.W., Stewart, S.T., Jacobsen, S.B., Mattsson, T.R., 2015. Impact vaporization of planetesimal cores in the late stages of planet formation. Nat. Geosci. 8, 269–272. https://doi.org/10.1038/ngeo2369.
Kresse, G., Furthmüller, J., 1996a. Efficiency of ab-initio total energy calculations for metals and semiconductors using a plane-wave basis set. Comput. Mater. Sci. 6, 15–50. https://doi.org/10.1016/0927-0256(96)00008-0.
Kresse, G., Furthmüller, J., 1996b. Efficient iterative schemes for *ab initio* total-energy calculations using a plane-wave basis set. Phys. Rev. B 54, 11169–11186. https://doi.org/10.1103/PhysRevB.54.11169.
Kresse, G., Joubert, D., 1999. From ultrasoft pseudopotentials to the projector augmented-wave method. Phys. Rev. B 59, 1758–1775. https://doi.org/10.1103/PhysRevB.59.1758.
Kubo, R., 1957. Statistical-mechanical theory of irreversible processes. I. General theory and simple applications to magnetic and conduction problems. J. Phys. Soc. Jpn. 12, 570–586. https://doi.org/10.1143/JPSJ.12.570.
Leopold, D.G., Lineberger, W.C., 1986. A study of the low-lying electronic states of Fe2 and Co2 by negative ion photoelectron spectroscopy. J. Chem. Phys. 85, 51–55. https://doi.org/10.1063/1.451630.
Li, Z., Caracas, R., Soubiran, F., 2020. Partial core vaporization during Giant impacts inferred from the entropy and the critical point of iron. Earth Planet. Sci. Lett. 547, 116463. https://doi.org/10.1016/j.epsl.2020.116463.
Marqués, M., González, L.E., González, D.J., 2015. *Ab initio* study of the structure and dynamics of bulk liquid Fe. Phys. Rev. B 92, 134203. https://doi.org/10.1103/PhysRevB.92.134203.
Mermin, N.D., 1965. Thermal properties of the inhomogeneous electron gas. Phys. Rev. 137, A1441–A1443. https://doi.org/10.1103/PhysRev.137.A1441.
Monkhorst, H.J., Pack, J.D., 1976. Special points for Brillouin-zone integrations. Phys. Rev. B 13, 5188–5192. https://doi.org/10.1103/PhysRevB.13.5188.
Nosé, S., 1984. A unified formulation of the constant temperature molecular dynamics methods. J. Chem. Phys. 81, 511–519. https://doi.org/10.1063/1.447334.
Perdew, J.P., Burke, K., Ernzerhof, M., 1996. Generalized gradient approximation made simple. Phys. Rev. Lett. 77, 3865–3868. https://doi.org/10.1103/PhysRevLett.77.3865.
Pierazzo, E., Vickery, A.M., Melosh, H.J., 1997. A reevaluation of impact melt production. Icarus 127, 408–423. https://doi.org/10.1006/icar.1997.5713.
Posner, E.S., Steinle-Neumann, G., Vlček, V., Rubie, D.C., 2017. Structural changes and anomalous self-diffusion of oxygen in liquid iron at high pressure. Geophys. Res. Lett. 44, 3526–3534. https://doi.org/10.1002/2017GL072926.
Pozzo, M., Davies, C., Gubbins, D., Alfè, D., 2012. Thermal and electrical conductivity of iron at Earth's core conditions. Nature 485, 355–358. https://doi.org/10.1038/nature11031.
Pozzo, M., Davies, C., Gubbins, D., Alfè, D., 2013. Transport properties for liquid silicon-oxygen-iron mixtures at Earth's core conditions. Phys. Rev. B 87. https://doi.org/10.1103/PhysRevB.87.014110.
Recoules, V., Renaudin, P., Clérouin, J., Noiret, P., Zérah, G., 2002. Electrical conductivity of hot expanded aluminum: experimental measurements and *ab initio* calculations. Phys. Rev. E 66, 056412. https://doi.org/10.1103/PhysRevE.66.056412.
Reed, M.S.C., Flurchick, K.M., 1994. Hybrid molecular dynamics: an approach to low density simulations. Comput. Phys. Commun. 81, 56–64. https://doi.org/10.1016/0010-4655(94)90110-4.
Stackhouse, S., Stixrude, L., Karki, B.B., 2015. First-principles calculations of the lattice thermal conductivity of the lower mantle. Earth Planet. Sci. Lett. 427, 11–17. https://doi.org/10.1016/j.epsl.2015.06.050.
Steinle-Neumann, G., Stixrude, L., Cohen, R.E., Gülseren, O., 2001. Elasticity of iron at the temperature of the Earth's inner core. Nature 413, 57–60. https://doi.org/10.1038/35092536.
Vočadlo, L., 2007. Ab initio calculations of the elasticity of iron and iron alloys at inner core conditions: evidence for a partially molten inner core? Earth Planet. Sci. Lett. 254, 227–232. https://doi.org/10.1016/j.epsl.2006.09.046.
Vočadlo, L., de Wijs, G.A., Kresse, G., Gillan, M., Price, G.D., 1997. First principles calculations on crystalline and liquid iron at Earth's core conditions. Faraday Discuss. 106, 205–218. https://doi.org/10.1039/a701628j.
Vočadlo, L., Alfè, D., Gillan, M.J., Wood, I.G., Brodholt, J.P., Price, G.D., 2003. Possible thermal and chemical stabilization of body-centred-cubic iron in the Earth's core. Nature 424, 536–539. https://doi.org/10.1038/nature01829.